L-Band radiative properties of vine vegetation at the MELBEX III SMOS Cal/Val Site

M. Schwank, J.-P. Wigneron, E. Lopez-Baeza, I. Völksch, C. Matzler, Yann H. Kerr

IEEE Transactions on Geoscience and Remote Sensing

L-Band Radiative Properties of Vine Vegetation at the SMOS Cal/Val Site MELBEX III

Journal:	*Transactions on Geoscience and Remote Sensing*
Manuscript ID:	Draft
Manuscript Type:	Regular paper
Keywords:	Radiometry, Vegetation, Calibration, Soil

L-Band Radiative Properties of Vine Vegetation at the SMOS Cal/Val Site MELBEX III

Mike Schwank[1], Jean-Pierre Wigneron[2], Ernesto Lopez-Baeza[3], Ingo Völksch[4], Christian Mätzler[5], Yann Kerr[2]

Abstract

Radiative properties at 1.4 GHz of vine vegetation were investigated by measuring brightness temperatures with the L-band radiometer ELBARA II operated on a tower at the MELBEX III field site in Spain. A reflecting foil was placed under the vines in their winter and summer states to measure brightness temperatures at horizontal and vertical polarization, which provide prevailingly information on vegetation transmissivities. The latter were retrieved from dual-polarized brightness temperatures measured at observation angles between 30° and 60° using a multiple scattering radiative transfer model. The analysis revealed practical parameter values that could be used to account for the impact of vine vegetation. The values are representative for the Mediterranean SMOS anchor station, and therefore valuable for the corresponding calibration and validation activities. Likewise, quantifying the uncertainties of the brightness temperatures measured was also important, especially as several equivalent ELBARA II instruments are currently operative in ongoing SMOS-related field campaigns.

1. Introduction

The terrestrial surface layer is an important boundary that controls energy and mass fluxes between the earth´s surface and the atmosphere. Techniques for monitoring the surface moisture are therefore of particular interest. Microwave radiometry at L band (1 – 2 GHz) is a passive remote sensing technique applicable for soil moisture retrieval at large scales [1-4]. On

[1] GFZ German Research Centre for Geosciences, Telegrafenberg, 14473 Potsdam, Germany, Section 5.1 "Geoecology and Geomorphology", mike.schwank@gfz-potsdam.de

[2] INRA, EPHYSE, Villenave d'Ornon, France

[3] University of Valencia, Department of Earth Physics and Thermodynamics, 46100 Valencia, Spain

[4] WSL Swiss Federal Institute for Forest, Snow and Landscape Research, 8903 Birmensdorf, Switzerland

[5] Institute of Applied Physics, University of Bern, Sidlerstrasse 5, 3012 Bern, Switzerland

2nd November 2009 the **S**oil **M**oisture and **O**cean **S**alinity (SMOS) satellite [5, 6] was launched as the **E**uropean **S**pace **A**gency's (ESA) second Earth Explorer Opportunity mission. The satellite carries the **M**icrowave **I**maging **R**adiometer using **A**perture **S**ynthesis (MIRAS) [7] on board to provide L-band brightness temperatures $T_B^{p,\alpha}$ at horizontal (p = H) and vertical (p = V) polarization at multiple observation angles α, with a spatial resolution of approximately 40 × 40 km^2 and near-global coverage. One of the primary goals of the SMOS mission is to produce global soil moisture maps with an accuracy better than 4 vol-% and a revisit time of less than three days [8]. The reliability of these land surface retrievals depends largely on the performance of the microwave emission models used to retrieve soil surface moisture from the multi-angular $T_B^{p,\alpha}$ measurements. Performing ground-based radiometer campaigns throughout the operative phase of the SMOS mission is therefore essential to validate and further improve the inversion algorithms based on radiative transfer modeling.

The **V**alencia **A**nchor **S**tation (VAS) in Spain was selected as the Mediterranean validation site for the SMOS-based retrievals of soil surface moisture and radiative properties of vegetation. These retrievals are routinely derived from $T_B^{p,\alpha}$, with an inversion scheme based on the τ-ω model that is the zero-order non-coherent solution of the radiative transfer equations [9]. It has been demonstrated that this model is adequate to reproduce $T_B^{p,\alpha}$ at L band (vacuum wavelength of ≈ 21 cm) emitted from vegetated sites [10-14], which makes it suitable for use in a multi-parameter inversion algorithm at feasible computational costs [13, 15, 16]. These findings, together with continuous refinements of the parameterization based on field experiments and simulations (e.g. [17-26]), led to the **L**-band **M**icrowave **E**mission of the **B**iosphere (L-MEB) inversion scheme [27], which is the current level-2 processor used to simultaneously derive soil moisture and vegetation opacity from multi-angular SMOS observations $T_B^{p,\alpha}$. However, some of the model parameters involved affect $T_B^{p,\alpha}$ rather similarly, which leads to some ambiguity in retrieving these parameters from L-MEB inversion using SMOS data. To overcome this problem, one option is to perform ground-based L-band radiometer campaigns under well-controlled

conditions, which yield $T_B^{p,\alpha}$ that are no longer simultaneously affected by some of these parameters.

Such a setup was used at the **M**editerranean **E**cosystem **L**-**B**and characterisation **EX**periment **III** (MELBEX III) field site at the Finca El Renegado, Caudete de las Fuentes (Valencia) Spain, which is fairly homogeneously covered with vineyards. Vineyards constitute approximately 75 % of the land use at the VAS which includes the MELBEX III site. While measuring the multi-angular $T_B^{p,\alpha}$ with the tower-based **E**TH **L**-**BA**nd **RA**diometer **II** (ELBARA II), a reflecting foil was placed underneath the vines to ensure that the sensitivity of the measurements to the emission of the soil below was very low. The $T_B^{p,\alpha}$ derived from these foil experiments were, therefore, predominantly affected by the vegetation, which meant it was possible to characterize the radiative properties of the vines in different development states. Such information is important for the ongoing SMOS calibration and validation activities at the VAS because: i) vegetation parameters retrieved with L-MEB from the $T_B^{p,\alpha}$ provided by the overflying MIRAS radiometer on board the SMOS satellite can be validated with the “ground truth” vegetation parameters derived from the ground-based measurements during foil experiments; ii) the “ground truth” vegetation parameters determined for the MELBEX III field site can be used in L-MEB to improve (or investigate) the accuracy of SMOS soil moisture retrievals for the VAS.

A further motivation for this study was to describe the MELBEX III site (Sections 2.1 and 2.2), and to investigate the long term performance of the ELBARA II radiometer deployed (Section 2.3). Since the MELBEX III site is an important anchor station for the SMOS mission, and since further identical ELBARA II instruments are currently deployed in other SMOS relevant campaigns, the analysis of a first long time series of tower-based $T_B^{p,\alpha}$ measurements is relevant because: i) the calibration strategy applied to produce the ground-based $T_B^{p,\alpha}$ must be analyzed and refined according to the findings; ii) uncertainties $\Delta T_B^{p,\alpha}$ of the calibrated $T_B^{p,\alpha}$ must be quantified so that they can be used for the SMOS validation. A detailed description of the foil experiments carried out to retrieve vegetation radiative properties was presented in Section 2.4.

In Section 3.1 the uncertainties $\Delta T_B^{p,\alpha}$ of $T_B^{p,\alpha}$ were estimated so that they could be taken into account in future SMOS calibration and validation activities based on ELBARA II. These uncertainties constrain the errors in the vegetation radiative properties derived from the measurements during the foil experiments (Section 3.2). Section 4 describes the derivation of the vegetation radiative properties from the multi-angular $T_B^{p,\alpha}$ and the air temperatures T_{air} measured during foil experiments on the basis of a multiple scattering radiative transfer model. The resulting retrievals of vegetation transmissivities and optical depths for distinctly different developmental states of the vines are presented in Section 5, and a summary and conclusions are given in Section 6.

2. The MELBEX III experiment

Here the MELBEX III field site for the study is described and a sketch of the auxiliary "ground truth" information available for the site is given. Although these data were not used in this analysis, they were included to provide a reference for the MELBEX III campaign, since this campaign plays a cardinal role in the ongoing SMOS calibration and validation activities. For the same reason the remote sensing system used is described rather extensively in Section 2.3, as is the setup of the foil experiments (Section 2.4) performed to derive L-band vegetation radiative properties.

2.1. General set-up

The VAS site is located about 80 km west of the city of Valencia (Spain) on the Utiel-Requena Plateau at 813 m a.s.l.. It was selected by the SMOS science team for the calibration and validation of SMOS data for the Mediterranean area as the landscape is relatively homogeneous over about 50 × 50 km^2, which is large enough to include at least one SMOS pixel. The predominant land-use types are vineyards (75%) and other Mediterranean ecosystem species such as shrubs, olive and almond trees, and pine forests. The topography is generally flat (slope angle < 2%), with some slightly undulating regions (8% - 15%). The surface air temperature

ranges from -15 ºC in winter to 45 ºC in summer, with an annual mean temperature of 14 ºC. The mean annual precipitation is about 450 mm, with peaks in spring and autumn.

The passive L-band measurements used in this study were performed at the MELBEX III site, which is part of the VAS. The data measured allow soil surface moisture and vegetation parameters to be upscaled for the entire VAS area for comparison with L-MEB retrievals based on SMOS data. In particular, dedicated short-term experiments were performed in which soil emission was largely shielded by means of a reflecting foil placed underneath the vine vegetation (referred to as “foil experiments”) to measure $T_B^{p,\alpha}$, which mainly carries information on vegetation radiative properties.

Figure 1a shows the ELBARA II radiometer mounted on the tower during a foil experiment, with a corresponding sketch in a bird´s eye view in panel b). The distances between the vines within a row were 2.00 – 2.10 m, and between rows 2.90 – 3.00 m. The MELBEX III vineyard studied belongs to the typical Spanish “tempranillo” variety and is representative of the entire VAS area. Panel c) is a photo of the site during the foil experiment in winter and panel d) in summer when the vegetation was fully developed. In the winter state, the vines are heavily trimmed to keep just the stocks with main branches fixed to wires along the rows. Typically, the first leaves start appearing at the beginning of May, and grape harvesting begins in the last week of September. Several field campaigns were performed to measure the **L**eaf **A**rea **I**ndex (*LAI*) of the developed vines and to determine the effective column densities of the **V**olumetric **W**ater **C**ontents (*VWC*) of different vegetation elements (stocks, grapes, stems, leaves). These values are given and used in Section 5.2 to derive estimates of effective vegetation radiative properties, which were compared with corresponding remotely sensed values.

Since the installation of the L-band radiometer ELBARA II [28] in September 2009 at the MELBEX III site, brightness temperatures $T_B^{p,\alpha}$ at polarization p = H, V and incidence angles 30° $\leq \alpha \leq$ 70° have been measured automatically in steps of 5° every 30 minutes. In contrast, at α = 45°, $T_B^{p,\alpha}$ are recorded every 10 minutes. Simultaneously with each $T_B^{p,\alpha}$ measurement, air temperature T_{air} is recorded right next to the radiometer to provide the only physical temperature

used in our analysis. Furthermore, every day around midnight sky radiances T_{sky} are measured at the nadir angle α_{sky} = 150° to recalibrate the ELBARA II **A**ctive **C**old noise **S**ource (ACS) used for internal calibration.

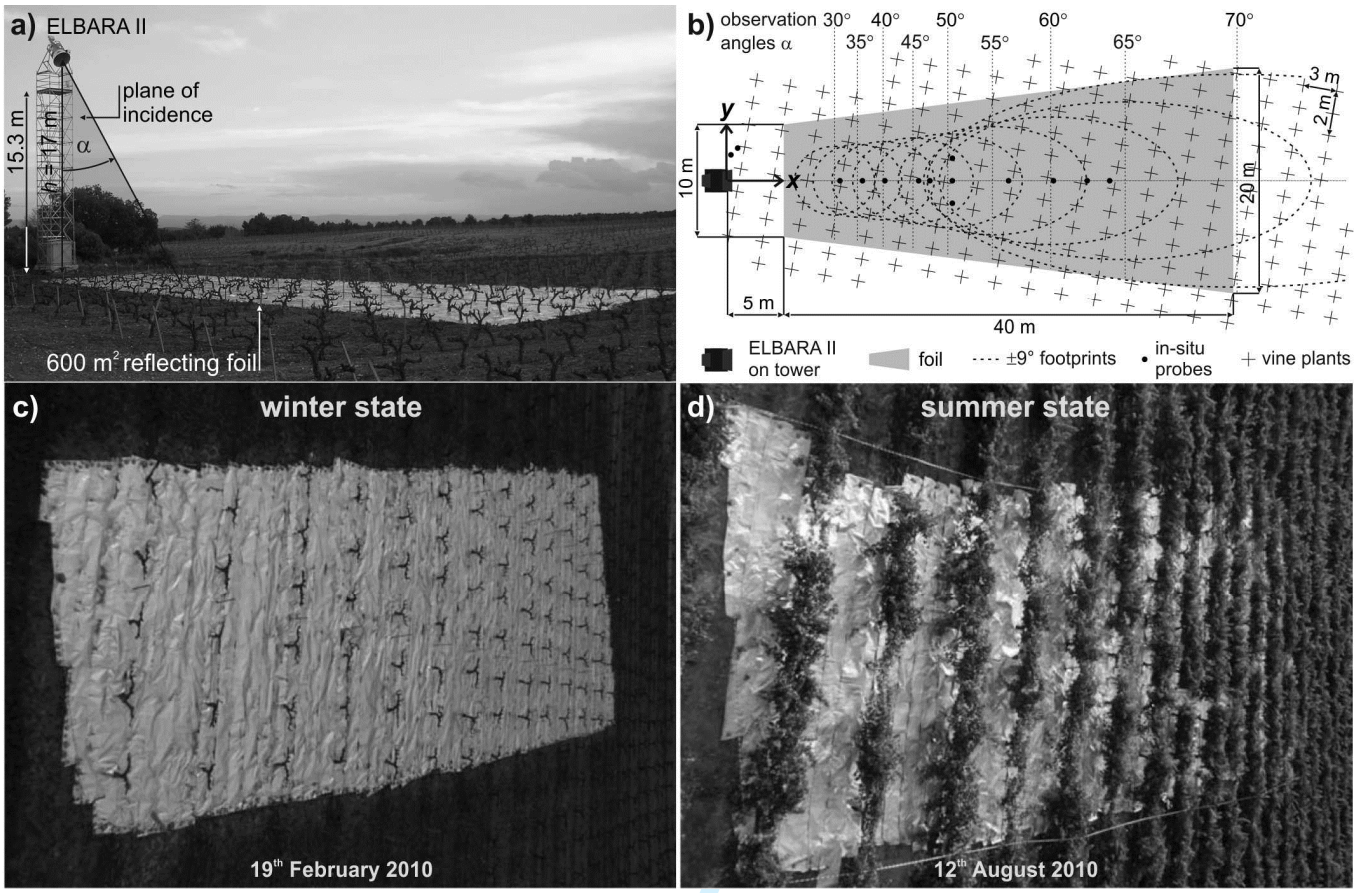

Figure 1: *a) Picture of the MELBEX III site during a foil experiment with the L-band radiometer ELBARA II mounted on the tower. b) Bird´s eye view of the configuration used in the foil experiments. Bold dots indicate the locations of the in-situ soil measurements, crosses the individual vines, and dashed ellipses the footprints observed at the different elevation angles α. c) and d) Photos of the sites prepared to investigate the winter state of the vegetation and its fully developed summer state on the basis of the $T_B^{p,\alpha}$ measured.*

2.2. Auxiliary data

The following auxiliary “ground truth” information is available for the MELBEX III site and relevant for the ongoing SMOS calibration and validation activities at the VAS area.

i) Time-series of precipitation measured every 15 minutes are available from the Jucar River Basin Authority rain gauge approximately 2 km from the MELBEX III site. Complementary meteorological data with a temporal resolution of 10 minutes are available from the VAS meteorological station situated at the Finca Cañada Honda, Bodegas Iranzo, about 4 km from the MELBEX III site.

ii) Soil moisture within the topmost 6 cm is measured in-situ every 10 minutes within the ELBARA II footprints using capacitive ThetaProbes (Delta-T Devices Ltd., type ML2x, nominal accuracy ±1%). To acquire surface soil moisture representative of the ELBARA II footprints, probes were installed on bare soil between vine rows and underneath the vines, close to the stumps (black dots in Figure 1b). Site-specific calibration was used to derive volumetric moisture from raw sensor data.

iii) Next to the tower base, a small network of additional moisture and temperature probes was installed (ThetaProbes; a Profile Probe, Delta-T Devices Ltd., type PR2) to monitor soil moisture at 4 depths down to 80 cm, and LI-COR sensors to measure soil temperatures at the depths 5, 10, 20, 30, 50 and 80 cm below the ground.

iv) A compact DAVIS Vantage Pro meteorological station is attached to the ELBARA II tower 2 m above ground to monitor air temperature, atmospheric humidity, pressure, wind speed and wind direction every 10 minutes.

2.3. Remote sensing system

The L-band radiometer ELBARA II [28] deployed at the MELBEX III site is the successor of the **E**TH **L**-**BA**nd **RA**diometer for soil-moisture research (ELBARA) [29], designed and built by the Institute of Applied Physics, University of Berne, Switzerland. Since further ground-based radiometer campaigns during the SMOS commissioning phase and during the operative phase of the mission appeared to be needed, three identical ELBARA II radiometer systems were requested by ESA and currently operative in SMOS relevant field campaigns.

ELBARA II was designed to be sensitive within the protected part 1400−1427 MHz of the microwave L band (1000–2000 MHz). Since the receiver bandwidth $B \approx 22$ MHz (at -3 dB) was narrow, the received noise power emitted from a site at the physical temperature $T \approx 300$ K may be as low as $P = k \cdot T \cdot B \approx 10^{-13}$ W. Low-noise amplifiers and a series of passive components with the net gain of 69 dB were implemented in the ELBARA II **M**icrowave **A**ssembly (MA). This was required to amplify the low input power to a level that matches the operational range of the power

detector used, so that voltages U could be generated at the output of the **P**ower **D**etector **A**ssembly (PDA) as linear responses to the input noise power. Furthermore, a sophisticated thermal system was developed to ensure the thermal stabilization of the electronics was accurate as this is crucial for long-term applications under widely varying environmental conditions.

Another challenge for the ELBARA II design was the internal calibration to derive $T_B^{p,\alpha}$ from instrumental raw data. This was solved by periodically switching between different reference noise sources fed to the radiometer MA, while recording the responses U at the output of the PDA. A **R**esistive noise **S**ource (RS) stabilized at the temperature $T_{RS} > T_B^{p,\alpha}$ was used for the hot calibration source, yielding the reference response U_{RS} at the PDA. The implementation of an **A**ctive **C**old **S**ource (ACS) to generate a cold reference noise temperature $T_{ACS} < T_B^{p,\alpha}$ with the associated PDA response U_{ACS} was another of the innovations implemented in ELBARA II. The noise temperature $T^p_{RM,\,in}$ at the radiometer input ports for H- and V-polarization were derived from the associated responses U^p using the linear interpolation between the reference responses of the RS and the ACS with known noise temperatures of $T_{ACS} \approx 37.8$ K and $T_{RS} \approx 313$ K (see subsection a) below).

$$T^p_{RM,\,in} = \frac{T_{RS} - T_{ACS}}{U_{RS} - U_{ACS}}\left(U^p - U_{ACS}\right) + T_{ACS} \qquad \text{and} \qquad T_B^{p,\alpha} = \frac{T^p_{RM,\,in} - \left(1 - t_{FC}\right)T_{FC}}{t_{FC}} \tag{1}$$

However, the experimentally relevant $T_B^{p,\alpha}$ entering the antenna aperture was slightly smaller than $T^p_{RM,\,in}$ due to the noise added by the lossy **F**eed-**C**able (FC) with transmissivity $t_{FC} < 1$. This was taken into account in the second equation in (1) that corrects $T^p_{RM,\,in}$ for the noise added by the FC at the temperature T_{FC}. To avoid error-prone extrapolation in deriving $T^p_{RM,\,in}$ from (1), the noise levels of the internal calibration sources were designed to fulfill $T_{RS} > T^p_{RM,\,in} > T_{ACS}$, which significantly increased the absolute accuracy of $T^p_{RM,\,in}$.

The technical details for the ELBARA II system are given in [28], but the specific system performances, which are important from the experimental point of view, are described in the

following subsections, drawing on experience in the field during the MELBEX III campaign. They are important for the harmonized operation of the different ELBARA II systems currently in use.

a) Noise reference sources

A 50 Ω RS stabilized at the instrument set-point temperature T_0 = 40 °C was used to provide the reference noise temperature $T_{RS} = T_0$ measured for the RS. For the time period from 19th February 2010 to 1st February 2011, the mean RS temperature was T_{RS} = 40 °C = 313.15 K, with a standard deviation of σT_{RS} < 0.08 K, and the mean system response was U_{RS} = 1.1089 V, with a standard deviation of σU_{RS} < 0.0002 V.

Since long-term experience with the novel ACS was lacking, diurnal recalibration at around midnight was needed using sky measurements where $T_{sky} < T_{ACS}$ and measurements on the RS where $T_{RS} > T_{ACS}$ (Section 3.1.4 in [28]). The ACS reference noise T_{ACS} was determined analogous to (1) (see Section 3.1.4 in [28]) with sky radiance T_{sky} computed with [30] for the elevation 750 m a.s.l. of the MELBEX III site and T_{air} measured. The mean T_{ACS} determined for the experimental time period was T_{ACS} = 37.83 K, with a standard deviation of σT_{ACS} = 0.63 K. The associated mean system response was U_{ACS} = 0.4711 V, with a standard deviation of σU_{ACS} < 0.0001 V. These observations indicate that the thermal stabilization of ELBARA II was excellent when it was operated under environmental conditions with air temperatures ranging from -3 °C < T_{air} < 35 °C. They also imply that the ACS is stabil in the long term, which allows significantly longer cycles to be applied for the recalibration of the ACS with sky measurements.

b) Treatment of radio frequency interferences

Radio **F**requency **I**nterference (RFI) can occur even within the protected 1400–1427 MHz band, which is the sensitive frequency range of ELBARA II. Hence, RFI was reduced by narrow-band filtering at the radiometer input (before amplification). Two strategies were used to detect RFI: (i) Narrow-band continuous RFI was detected by splitting the protected band into a **L**ower **S**ide **B**and (LSB) and an **U**pper **S**ide **B**and (USB). The **F**requency-**D**omain (FD) criterion $FD \equiv \left| T^p_{\mathrm{B,\,USB}} - T^p_{\mathrm{B,\,LSB}} \right|$, with a threshold *FD* = 0.4 K, was used to detect narrow-band RFI. (ii) Bursts

of RFI were detected by analyzing the time series of noise power measured at the rate of 800 Hz. It was expected that the inherent Gaussian statistics associated with undisturbed thermal noise would be altered by RFI bursts, so that these bursts could be detected by checking kurtosis *k* [31, 32], which is *k* = 3 for a perfect Gaussian distribution. Consequently, the **T**ime-**D**omain (*TD*) criterion $TD \equiv |k-3|$ was defined to identify RFI bursts. The corresponding threshold value was determined on the basis of the responses U_{RS} measured at the PDA output, when the internal RS was switched to the receiver path. As expected, the kurtosis of these undisturbed measurements was $k_{RS} = 3$, with a standard deviation $\sigma k_{RS} < 0.1$. This value is considered as the instrumental limitation, which led us to set the threshold to $TD = 3 \cdot \sigma k_{RS} \approx 0.3$ for the antenna measurements.

c) Antenna and radiometer mount

The ELBARA II system is mounted on a tower 15.3 m above the ground (Figure 1a). The system is equipped with an elevation tracker that allows the antenna to be oriented automatically for 30° ≤ α ≤ 330° with α = 180° as the zenith direction (Section 2.4. in [28]). After the system was installed on the tower, the elevation tracker was calibrated with a digital level to achieve reproducible α with an absolute accuracy better than ±1°. In the MELBEX III campaign, measurements were taken at 30° ≤ α ≤ 70° with steps of 5°, whereas only $T_B^{p,\alpha}$ measured for 30° ≤ α ≤ 60° were used to explore the vegetation radiative properties based on the foil experiments. At the intermediate angle α = 45° the center of the antenna beam waist is approximately 1.7 m above the base of the ELBARA II scaffold, leading to the height *h* = 17 m, which was used to compute the size (Figure 1b) and the fractional amounts μ^{α} (Section 2.4) of the footprints for the different α. The latter required knowing the antenna relative sensitivity *D*(Θ) with respect to the antenna main direction, for which *D*(Θ = 0°) = 1. While the system was being constructed, *D*(Θ) was derived experimentally by measuring the sun disk moving through the field of view of the antenna (Section 3.2.1 in [28]). For Θ ≤ 15°, these data were approximated with the following Gaussian bell curve (Θ in °):

$$D(\Theta) = \exp\left(-0.01781 \cdot \Theta^2\right) \quad (2)$$

In agreement with the rotational symmetry of the Pickett-horn [33] antenna in the ELBARA II system, $D(\Theta)$ depends exclusively on the polar angle Θ. This implies that (2) holds for both polarizations received with the two orthogonal $\lambda/4$-structures implemented in the antenna feed (see Section 2.3 in [28]).

2.4. Foil experiments

The role of the MELBEX III site as the Mediterranean SMOS ground-truth site required dedicated short-term experiments to separate the radiances originating from the vegetation from those emitted by the soil below. To ensure that measured $T_B^{p,\alpha}$ predominantly carried information on vegetation transmissivities $\Gamma^{p,\alpha}$ and optical depths $\tau^{p,\alpha}$, soil emission was shielded by placing a reflecting foil below the vegetation (Figure 1). Hence, approximately 600 m^2 of metalized foil[6] was spread out in the trapezoidal shape depicted in Figure 1b to prevent any soil emission from this area.

The dashed ellipses in Figure 1b indicate the projection of the ±9° beam angles onto the footprint plane from which the fractional amounts $\mu^\alpha > 0.93$ of the total radiance should originate for α = 30°, 35°, 40°, 45°, 50°, 55°, 60° for a homogeneous footprint. However, due to the trapezoidal shape of the foil, values μ^α for given α and the height h = 17 m of the beam waist were computed numerically for this specific setup, taking into consideration the normalized antenna sensitivity $D_N(\Theta^{\alpha,h,\delta})$ derived from (2) and the angle δ representing a possible misalignment of the antenna in azimuth direction:

$$\mu^\alpha = \iint_{\text{foil area}} D_N\left(\Theta^{\alpha,h,\delta}(x,y)\right) \cdot d\Omega^{h,\delta}(x,y,dx,dy) \quad (3)$$

[6] The composite foil is made up of a 12-μm-thick aluminum film inbetween 12 μm of polyester and 75 μm of polyethylene. The thickness of the electrically conductive and paramagnetic aluminum is significantly larger than the skin depth at L band, implying that perfect reflectivity (and hence perfect shielding of the soil emission) can be assumed for the area covered with the foil.

Omitting the algebraic details along with the coordinate transformations and vector geometry, $\Theta^{\alpha,h,\delta}(x,y)$ represents the angle between the antenna main direction at α, h, δ and the view direction of a point in the xy-footprint plane. Seen from the perspective of the radiometer, the solid angle $d\Omega^{h,\delta}(x,y,dx,dy)$ covers an infinitesimal area $dx \cdot dy$, located at a position (x, y) in the footprint plane. The surface integral in (3) was evaluated numerically, yielding the angular dependency of μ^{α} shown in Figure 2. The error bars indicate results from evaluations performed for $\delta = \pm 3°$, which is large enough to include the possible misalignment of the radiometer in azimuth direction.

All configurations considered in the simulations reveal $\mu^{\alpha} > 0.93$, with a maximum of $\mu^{\alpha} = 0.997$ at $\alpha = 35°$. For shallower observations, μ^{α} decreases and misalignments δ become more relevant, as expected. However, the impact of radiance originating from areas outside the foil-covered part of the footprint on $T_B^{p,\alpha}$ was expected to be very small due to the generally high values μ^{α} (compare Section 4.1), which implies that uncertainties in the emission of these areas would not significantly affect the retrieved vegetation radiative properties described in Section 5.1.

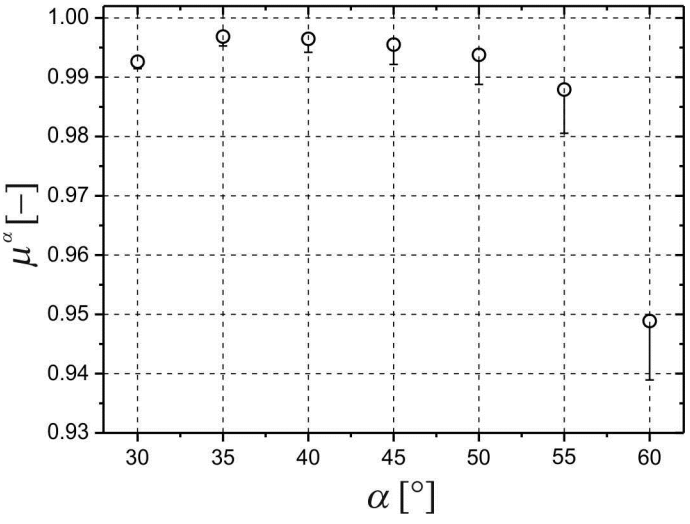

Figure 2: *Computed fractional amounts μ^{α} of radiance originating from the foil-covered (trapezoidal) area (Figure 1b) on a homogeneous footprint at observation angle α. Error bars $\Delta\mu^{\alpha}$ were computed for a misalignment of the antenna in azimuth direction of $\delta = \pm 3°$.*

3. Brightness temperatures

An error analysis of measured $T_B^{p,\alpha}$ to quantify the absolute uncertainties $\Delta T_B^{p,\alpha}$, was important for two reasons: i) to calibrate and validate SMOS data on the basis of ELBARA II measurements; ii) to constrain errors in the vegetation transmissivities $\Gamma^{p,\alpha}$ and optical depth $\tau^{p,\alpha}$ (Section 5) derived from the $T_B^{p,\alpha}$ measured during the foil experiments (see Section 3.2).

3.1. Uncertainties associated with the brightness temperatures measured

As described in Section 2.3, the equations (1) were used to derive $T_B^{p,\alpha}$ from instrumental raw data. To achieve conservative estimates for the corresponding uncertainties $\Delta T_B^{p,\alpha}$ and to take into account the fact that some of the error-prone parameters involved are not correlated with any of the other parameters (e.g. T_{FC}), arithmetic error propagation $\Delta T_B^{p,\alpha} = \sum \Delta X \cdot \left| \partial T_B^{p,\alpha} / \partial X \right|_{\{X\}}$ was applied in conjunction with (1). The summation was performed over the individual parameters involved in (1), and summarized with the symbol $\{X\} \equiv \{T_{RS}, T_{ACS}, U_{RS}, U_{ACS}, U^{p,\alpha}, T_{FC}, t_{fc}\}$, with associated uncertainties $\{\Delta X\} \equiv \{\Delta T_{RS}, \Delta T_{ACS}, \Delta U_{RS}, \Delta U_{ACS}, \Delta U^{p,\alpha}, \Delta T_{FC}\}$. The values of $\{X\}$ and $\{\Delta X\}$ used in the error propagation analysis were derived from the approximately $150 \cdot 10^3$ ELBARA II measurements performed between 19th February 2010 and 1st February 2011 (Section 2). shows the values $\{X\}$ and $\{\Delta X\}$ and summarizes their derivations (these are explained in more detail below).

The statistical uncertainties $\Delta U = \Delta U_{RS}$, ΔU_{ACS}, and $\Delta U^{p,\alpha}$ of the PDA responses (voltages) $U = U_{RS}$, U_{ACS}, and $U^{p,\alpha}$ were computed from the standard deviations σU of these measurements associated with corresponding noise-power levels $T_{RM\,in} = T_{RS}$, T_{ACS}, and $T_B^{p,\alpha}$, performed with the shortest possible integration time 2.5 ms of ELBARA II. Equation (12) in [28] was used with the system parameters (radiometer gain G_{RM} = 1.86 mV K^{-1}, radiometer residual noise $T_{RM,\,0}$ = 153 K, time-bandwidth product $B\tau$ = 15868 Hz s, PDA noise σU_{PDA} = 0.649 mV) determined experimentally during the construction of ELBARA II (Table 2 in [28]). Finally, the three values ΔU used with the arithmetic error propagation were computed as $\Delta U = \sigma U \cdot (f_{LP} \cdot \tau_{rec})^{-1/2}$ with f_{LP} =

400 Hz as the cut-off frequency of the PDA, and the integration time τ_{rec} = 3 s applied to our measurements (corresponding to 1200 independent measurements with 2.5 ms integration time each).

The mean physical temperature T_{FC} of the **F**eed **C**able (FC) was approximated with T_{air} measured next to the FC simultaneously with the $T_B^{p,\alpha}$. The assumed uncertainty, ΔT_{FC} = 5 K, accounts for the temperature variations along the FC connecting the receiver with the antenna ports, which are not of course, taken into account in the simple model (1) used to correct for FC noise. The value of the FC transmission t_{FC} = 0.977 results from its specified loss L_{FC} = 0.1 dB (Section 2.2.1 in [28]). As this value can be considered constant, at least for the period between two sky calibrations, the uncertainty Δt_{FC} = 0 is assumed.

Table 1: *Values and comments on the parameters* $\{X\} \equiv \{T_{RS}, T_{ACS}, U_{RS}, U_{ACS}, U^{p,\alpha}, T_{FC}, t_{fc}\}$ *with uncertainties* $\{\Delta X\} \equiv \{\Delta T_{RS}, \Delta T_{ACS}, \Delta U_{RS}, \Delta U_{ACS}, \Delta U^{p,\alpha}, \Delta T_{FC}\}$ *used to compute* $\Delta T_B^{p,\alpha}$ *shown in Figure 3*

$\{X\}$	$\{\Delta X\}$	Comments
T_{RS} = 313 K	ΔT_{RS} = σT_{RS} = 71 mK	Mean internal physical temperature, measured with associated standard deviation (Section 2.3a)
U_{RS} = 1.11 V	ΔU_{RS} = σU_{RS} = 199 μV	Mean PDA response (voltage) for the RS with associated statistical uncertainty σU_{RS} (Section 2.3a)
T_{ACS} = 37.8 K	ΔT_{ACS} = σT_{ACS} = 631 mK	Mean ACS temperature, derived from sky calibrations with associated standard deviation (Section 2.3a)
U_{ACS} = 0.471 V	ΔU_{ACS} = σU_{ACS} = 83 μV	Mean PDA response (voltage) for the ACS with associated standard deviation σU_{ACS} (Section 2.3a)y
$U^{p,\alpha}$ = *0.75 V – 1.21 V*	$\Delta U^{p,\alpha}$ = $\sigma U^{p,\alpha}$	Mean PDA response (voltage) for antenna measurements with associated statistical uncertainty $\sigma U^{p,\alpha}$ (Section 2.3a)
T_{FC} = 14.5°C	ΔT_{FC} = 5 K	Mean T_{air} measured with estimated temperature difference at along the FC
t_{FC} = 0.977	Δt_{FC} = 0	Specified FC transmissivity

The absolute uncertainties $\Delta T_B^{p,\alpha}$ computed with arithmetic error propagation applied to (1) also depend on the values of $T_B^{p,\alpha}$ measured. Hence, $\Delta T_B^{p,\alpha}$ (Figure 3) are estimated for the

range 0 K ≤ $T_B^{p,\alpha}$ ≤ 370 K to represent all the situations at horizontal and vertical polarization observed during the foil experiments, as well as during the measurements performed on the undisturbed vineyard. Considering the corresponding ranges of $T_B^{p,\alpha}$ (large arrows in Figure 3), the range of uncertainty expected for $T_B^{p,\alpha}$ measured with the reflecting foil below the vine vegetation was 0.69 K < $\Delta T_B^{p,\alpha}$ < 0.94 K, and 0.57 K < $\Delta T_B^{p,\alpha}$ < 0.74 K for the measurements on the undisturbed vineyard.

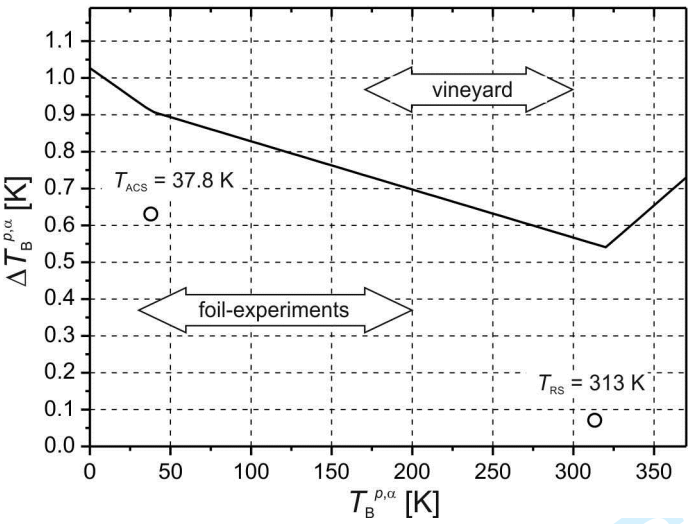

Figure 3: *Uncertainties $\Delta T_B^{p,\alpha}$ of $T_B^{p,\alpha}$ measured with ELBARA II. The noise temperatures, T_{ASC} and T_{RS}, of internal reference sources, and ranges of $T_B^{p,\alpha}$ measured during the foil experiments and on the undisturbed vineyard are indicated.*

3.2. Brightness temperatures measured during the foil experiments

Since ELBARA II was commissioned in September 2009, it has provided calibrated $T_B^{p,\alpha}$ for p = H, V and 30° ≤ α ≤ 70° that are currently being analyzed within the framework of the ongoing SMOS calibration and validation activities. While the reflecting foil has been laid out, sequences of $T_B^{p,\alpha}$ were measured for 30° ≤ α ≤ 60° to derive transmissivities $\Gamma^{p,\alpha}$ and optical depths $\tau^{p,\alpha}$ with different vegetation states (Section 5). Comparable measurements of $T_B^{p,\alpha}$ at the vineyard with similar vegetation states and without any foil below the vines were used to comprise the combined emissions of vegetation and soil (Section 4.1, equation (7)). Figure 4 shows the data sequences *T*ws_f, *T*ws_nf and *T*ss_f, *T*ss_nf, where “ws” refers to the **w**inter **s**tate of the

vineyard and “ss” indicates the **s**ummer **s**tate. The index “f” indicates the periods when the **f**oil was under the vines and “nf” refers to the periods when **n**o **f**oil was under the vines with the same developmental states. The bottom rows in Figure 4 show air temperatures T_{air} measured next to the radiometer at the same time as the $T_B^{p,\alpha}$.

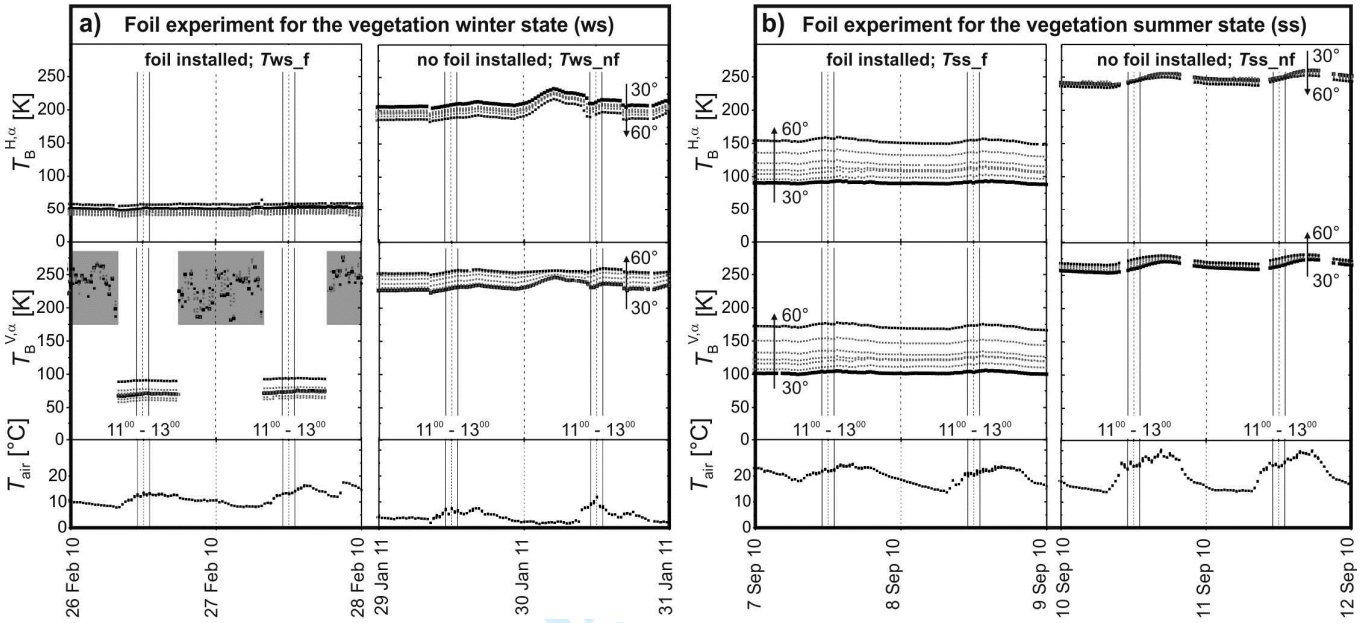

Figure 4: *Time series of $T_B^{p,\alpha}$ measured for p = H, V and α = 30° (bold black), 35° 40°, 45°, 50°,55° (gray), 60° (black). Arrows indicate trends of angular dependencies of $T_B^{p,\alpha}$. Gray shaded boxes indicate RFI distorted $T_B^{V,\alpha}$. The data used to derive the radiative properties of the vegetation´s winter state and its fully developed state are constrained to time periods between 11^{00} and 13^{00} indicated in a) and b), respectively. $T_B^{p,\alpha}$ measured with the foil on the soil are shown in the left columns of a) and b). The right columns show $T_B^{p,\alpha}$ of the vineyard without the foil below the vines with the same vegetation states. The bottom rows show T_{air} measured on the tower at the same time as $T_B^{p,\alpha}$.*

During the period *T*ws_f, distinct RFI was observed exclusively at V-polarization every day between 19^{00} and 7^{30} (indicated by the gray shaded boxes). The data from the four two-day periods *T*ws_f (26. – 27. February 2010), *T*ws_nf (29. – 30. January 2011) and *T*ss_f (7. – 8. September 2010), *T*ss_nf (10. – 11. September 2010) were further constrained to the hours 11^{00} – 13^{00} for analysis because this measure improves the comparability between $\Gamma^{p,\alpha}$ and $\tau^{p,\alpha}$ retrieved for different vegetation states. Moreover, the RFI-distorted periods had to be excluded from the analysis.

The $T_B^{p,\alpha}$ shown in Figure 4 differ significantly for all time periods *T*ws_f, *T*ws_nf and *T*ss_f, *T*ss_nf. Qualitatively, the angular dependence of the $T_{B,}^{p,\alpha}$ measured for the winter state of the vineyard with no foil (*T*ws_nf) corresponds to the emission expected for a specular (Fresnel)

surface ($T_B^{V,\alpha} > T_B^{H,\alpha}$ and decreasing $T_B^{H,\alpha}$ with increasing α, while $T_B^{V,\alpha}$ increases with α). In contrast, the sensitivity of $T_B^{p,\alpha}$ with respect to α is generally less pronounced during the undisturbed vegetation summer state (*T*ss_nf) and some of the $T_B^{p,\alpha}$ even respond in the opposite way. The $T_B^{p,\alpha}$ measured for the vegetation winter state with the foil (*T*ws_f) were rather small (35 K < $T_B^{p,\alpha}$ < 100 K) and no clear trend with α can be identified. Again, with the summer vegetation state and the foil (*T*ss_f), the behavior was significantly different. Here the $T_B^{p,\alpha}$ increased with α at both polarizations, and the sensitivity with respect to α distinctly increased in comparison with the period Tws_f during the vegetation winter state with the foil. In summary, the state of the vegetation became primarily apparent in the angular dependencies of the $T_B^{p,\alpha}$ measured, as well as in the overall magnitudes.

4. Modeling approach

The following sub-sections describe the models used to quantify transmissivities $\Gamma^{p,\alpha}$ and optical depths $\tau^{p,\alpha}$ of the vegetation at different developmental stages for H- and V- polarization on the basis of the $T_B^{p,\alpha}$ and T_{air} shown in Figure 4.

4.1. Microwave radiative transfer

The thermal L-band emissions $T_B^{p,\alpha}$ of the vineyards during the periods with no foil (periods *T*ws_nf and *T*ss_nf in Figure 4) are modeled with the very simple radiative transfer approach (4). It uses the merged reflectivity $R^{p,\alpha}_{vine}$ of the vine vegetation and soil and the effective temperature T_{vine} of the vineyard, and assumes that the temperature is the same all over the site:

$$T_B^{p,\alpha} = \left(1 - R_{vine}^{p,\alpha}\right) T_{vine} + R_{vine}^{p,\alpha} T_{sky} \quad (4)$$

Modeling $T_B^{p,\alpha}$ of areas with the highly reflective foil underneath the vines requires a more sophisticated approach. With increasing ground reflection, multiple reflections across the vegetation become increasingly relevant, and the zero-order scattering model [34], also called the τ - ω model [9, 35, 36], is therefore not an appropriate choice. To account for multiple

reflections, we use the multiple-scattering approach (5) described in [37, Section 4.2.5.1] to model $T_B^{p,\alpha}$ emitted from areas with the reflecting foil. In (5), T_G and T_V are the effective temperatures of the ground and the vegetation, and $R_G^{p,\alpha}$ is the ground reflectivity:

$$T_B^{p,\alpha} = T_G a_G + T_V a_V + T_{sky}\left(1 - a_G - a_V\right) \quad \text{with}$$
$$a_G = t_V \frac{1 - R_G^{p,\alpha}}{1 - R_G^{p,\alpha} r_V} \tag{5}$$
$$a_V = (1 - r_V - t_V)\frac{1 + R_G^{p,\alpha}(t_V - r_V)}{1 - R_G^{p,\alpha} r_V}$$

The equations (4.13) and (4.14) in [37] define the reflectivity r_V and the transmissivity t_V of the scattering vegetation layer. For moderate scattering, these can be approximated with:

$$r_V = r_\infty\left(1 - \Gamma^{p,\alpha 2}\right) \text{ and } t_V = \Gamma^{p,\alpha}\left(1 - r_\infty^2\right) \text{ with } r_\infty \cong \frac{\omega^{p,\alpha}}{2} \tag{6}$$

Where the reflectivity r_∞ of the vegetation at infinite thickness is given by equation (4.16) in [37]. Considering that scattering in the backward hemisphere is much smaller than absorption, (4.17) [37] can be approximated with a corresponding first-order Taylor expansion. Using this approximation in (4.16) and considering the definitions (4.2) relates r_∞ to the effective scattering albedo $\omega^{p,\alpha}$, as it is expressed by the third relation in (6).

The denominators (1 - $R_G^{p,\alpha} \cdot r_V$) in (5) express the infinite reflections within the vegetation layer, which obviously become dominant if the ground is perfectly reflecting ($R_G^{p,\alpha}$ = 1) because of the metalized foil. Furthermore, it can easily be shown that this multiple-scattering emission model becomes equivalent to the zero-order τ - ω model for $\omega^{p,\alpha}$ = 0, which then represents non-scattering vegetation. Although the assumption $\omega^{p,\alpha}$ = 0 is often made for low growing vegetation types, this is not necessarily adequate for vineyards since grapevines have a significant amount of woody matter with dimensions comparable with the L-band wavelengths (≈ 21 cm). This is why we considered the range $0 \le \omega^{p,\alpha} \le 0.1$ in the analysis presented in Section 5.

The sky radiance T_{sky} used in (4) and (5) was computed with [30] for the elevation 750 m a.s.l. of the MELBEX III site, the T_{air} measured, and the direction of the downwelling T_{sky} received by

the radiometer after its forward reflection at the ground. For -3 °C < T_{air} < 40 °C and 30° ≤ α ≤ 60°, the associated sky brightness temperatures are in the range of 4.45 K ≤ T_{sky} ≤ 5.54 K. Furthermore, T_{air} measured was used for all the effective temperatures involved in (4) and (5), and the resulting errors are analyzed.

During the periods *T*ws_f and *T*ss_f, the $T_B^{p,\alpha}$ measured comprise contributions of radiances $T_{B,f}^{p,\alpha}$ and $T_{B,vine}^{p,\alpha}$ originating from the area with the reflecting foil, and from the adjacent undisturbed vineyard, respectively. The radiances, $T_{B,f}^{p,\alpha}$ and $T_{B,vine}^{p,\alpha}$, emitted from within the antenna´s field of view were weighted with the fractional amounts μ^α and (1 - μ^α), respectively, shown in Figure 2:

$$T_B^{p,\alpha} = \mu^\alpha T_{B,f}^{p,\alpha} + \left(1-\mu^\alpha\right) T_{B,vine}^{p,\alpha} \tag{7}$$

Where, (4) is used to represent $T_{B,vine}^{p,\alpha}$, and (5) and (6) is used to express $T_{B,f}^{p,\alpha}$ with $R_G^{p,\alpha}$ = 1 to represent the perfect reflection of the metallized foil.

4.2. Vegetation transmissivities and uncertainties

Vegetation transmissivities $\Gamma^{p,\alpha}$ were derived for the vegetation **w**inter **s**tate (ws) and the **s**ummer **s**tate (ss) from the $T_B^{p,\alpha}$ shown in Figure 4. The weighting approach (7), with the radiative transfer models (4), (5), and (6) is solved numerically for $\Gamma^{p,\alpha}$ with inserted $T_B^{p,\alpha}$ measured during the periods *T*ws_f and *T*ss_f. The effective physical temperatures, T_{vine} of the vineyard and T_V of the vegetation were both approximated with air temperatures T_{air} measured at the radiometer. Of course, the assumption, T_{vine} = T_V = T_{air} introduces certain errors that are estimated as ΔT_{vine} = ΔT_V = 5 K to represent upper limits. The uncertainties $\{\Delta Y\} \equiv \{\Delta\mu^\alpha, \Delta T_B^{p,\alpha}, \Delta T_V, \Delta T_{vinyard}, \Delta R^{p,\alpha}{}_{vine}, \Delta T_{sky}, \Delta\omega^{p,\alpha}\}$ of the parameters $\{Y\} \equiv \{\mu^\alpha, T_B^{p,\alpha}, T_V, T_{vine}, R^{p,\alpha}{}_{vine}, T_{sky}, \omega^{p,\alpha}\}$ involved in (7) (with (4), (5), and (6) substituted) were used with arithmetic error propagation to achieve conservative estimates of absolute uncertainties $\Delta\Gamma^{p,\alpha} = \sum \Delta Y \cdot \left|\partial\Gamma^{p,\alpha}/\partial Y\right|_{\{Y\}}$ of the transmissivities $\Gamma^{p,\alpha}$ (summation was performed over the parameters).

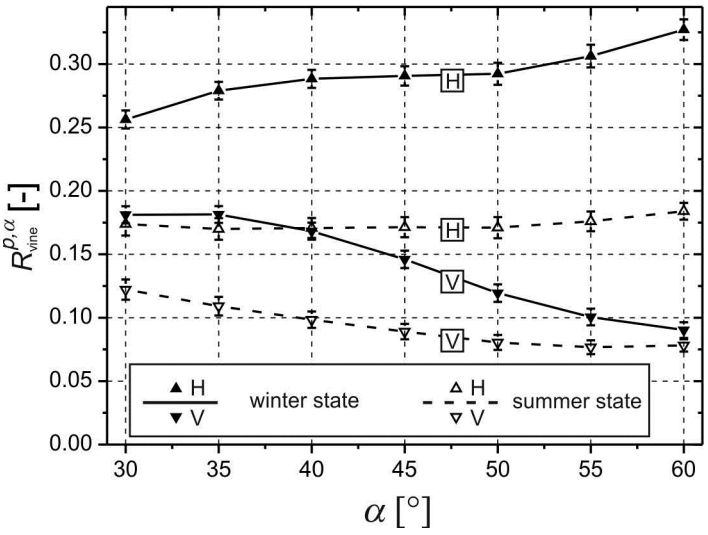

Figure 5: *Mean values of reflectivities $R^{p,\alpha}{}_{vine}$ of the vineyard for the winter and summer states derived from measurements performed during the periods Tws_nf und Tss_nf (Figure 4).*

The reflectivities of the vineyard outside the foil-covered area used in (4) were estimated as the mean values $R^{p,\alpha}{}_{\text{vine}}$ derived from the time-series of vineyard reflectivities deduced from measurements during the time periods *T*ws_nf and *T*ss_nf shown in the right columns in Figure 4 a) and b). The resulting $R^{p,\alpha}{}_{\text{vine}}$ for the winter- (solid symbols) and the summer state (empty symbols) at H-(up triangles) and V-polarization (down triangles) are depicted in . The angular dependency of $R^{p,\alpha}{}_{\text{vine}}$ observed for the winter state behaved similarly to what could be expected for a Fresnelian reflector, i.e. increasing $R^{H,\alpha}{}_{\text{vine}}$ with increasing α, and $R^{V,\alpha}{}_{\text{vine}}$ reaches a minimum when α approaches the Brewster angle. The $R^{p,\alpha}{}_{\text{vine}}$ of the vineyard during summer is clearly less sensitive to α, which is rather typical for a diffuse reflector. Hence, the $R^{p,\alpha}{}_{\text{vine}}$ demonstrate the marked effect of the vegetation state on the angular dependency of the L-band signatures even more distinctly than the measured $T_B{}^{p,\alpha}$ presented in Section 3.2. The error bars in represent standard deviations $\sigma R^{p,\alpha}{}_{\text{vine}}$ deduced for the time series of the vineyard reflectivities measured for the periods *T*ws_nf and *T*ss_nf (right columns in Figure 4 a) and b)), and were used to estimate the uncertainties $\Delta R^{p,\alpha}{}_{\text{vine}}$ of $R^{p,\alpha}{}_{\text{vine}}$.

As an upper limit for the uncertainty of the model-based sky radiance T_{sky}, we assumed ΔT_{sky} = 1 K. For μ^{α}, the values shown in Figure 2 were used together with the uncertainties $\Delta\mu^{\alpha}$

computed for a misalignment $\delta = \pm 3°$ between the radiometer plane of incidence and the symmetry axes of the trapezoidal foil. The uncertainties $\Delta T_B^{p,\alpha}$ of the measured $T_B^{p,\alpha}$ used to derive $\Gamma^{p,\alpha}$ were taken into account by the relation $\Delta T_B^{p,\alpha}(T_B^{p,\alpha})$ shown in Figure 3. The sensitivity of the $\Gamma^{p,\alpha}$ to the effective single-scattering albedo $\omega^{p,\alpha}$ was analyzed by considering the two values $\omega^{p,\alpha} = 0$ and $\omega^{p,\alpha} = 0.1$, which are believed to include the existing range of uncertainty. Brief comments on the origin of the parameters values $\{Y\}$ and the associated uncertainties $\{\Delta Y\}$ are given in Table 2.

Table 2: *Values and comments on the parameters* $\{Y\} \equiv \{\mu^\alpha, T_B^{p,\alpha}, T_V, T_{vine}, R^{p,\alpha}{}_{vine}, T_{sky}, \omega^{p,\alpha}\}$ *with uncertainties* $\{\Delta Y\} \equiv \{\Delta\mu^\alpha, \Delta T_B^{p,\alpha}, \Delta T_V, \Delta T_{vine}, \Delta R^{p,\alpha}{}_{vine}, \Delta T_{sky}, \Delta\omega^{p,\alpha}\}$ *used to derive* $\Gamma^{p,\alpha}$ *and* $\Delta\Gamma^{p,\alpha}$.

$\{Y\}$	$\{\Delta Y\}$	Comments
μ^α	$\Delta\mu^\alpha$	Computed values shown in Figure 2
$T_B^{p,\alpha}$	$\Delta T_B^{p,\alpha}$	Measured values (Figure 4) with uncertainties computed (Figure 3)
T_V = T_{air}	ΔT_V = 5 K	Measured values (Figure 4) with assumed uncertainty
T_{vine} = T_{air}	ΔT_{vine} = 5 K	Measured values (Figure 4) with assumed uncertainty
$R^{p,\alpha}{}_{vine}$	$\Delta R^{p,\alpha}{}_{vine}$ = $\sigma R^{p,\alpha}{}_{vine}$	Values measured during *T*ss_nf and *T*ws_nf () with standard deviations indicated
T_{sky}	ΔT_{sky} = 1 K	Computed with [30] and uncertainty assumed
$\omega^{p,\alpha}$ = 0 and 0.1	$\Delta\omega^{p,\alpha}$ = 0	Feasible range for the MELBEX III vineyard

4.3. Vegetation optical depth

Vegetation optical depths $\tau^{p,\alpha}$ along the view in the direction of the observation angle α and the optical depths $\tau_0^{p,\alpha}$ in the nadir direction, can be deduced from the corresponding transmissivities $\Gamma^{p,\alpha}$ using Beer´s law if isotropy of vegetation absorption can be assumed:

$$\tau^{p,\alpha} = -\ln\left(\Gamma^{p,\alpha}\right) \qquad \tau_0^{p,\alpha} = \tau^{p,\alpha} \cdot \cos\alpha \tag{8}$$

However, we have to take into account the fact that vegetation often shows bi-axial anisotropy [10, 13, 14, 38] [7]. In the L-MEB model [27], vegetation anisotropy is accounted for by using the following empirical approach:

$$\tau_0^p(\alpha) = \tau_{\mathrm{NAD}}\left[tt^p \cdot \sin^2\alpha + \cos^2\alpha\right] \tag{9}$$

The parameters τ_{NAD} and tt^p (p = H, V) were determined simultaneously in L-MEB retrievals by applying an optimization approach to multi-angular $T_B^{p,\alpha}$-data measured, e.g., with SMOS. In Section 5.2, τ_{NAD} and tt^p are quantified according to ground-based measurements that can be compared with the corresponding L-MEB retrievals from SMOS measurements over the VAS site. These "ground truth" values of the parameters τ_{NAD}, tt^{H}, tt^{V} involved in $\tau_0^p(\alpha)$ given by (9) are determined by minimizing the objective function OF (summation is over the observation angles α measured):

$$OF = \sum_{\alpha}\left[\left(\tau_0^{\mathrm{H}}(\alpha) - \tau_0^{\mathrm{H},\alpha}\right)^2 + \left(\tau_0^{\mathrm{V}}(\alpha) - \tau_0^{\mathrm{V},\alpha}\right)^2\right] \tag{10}$$

5. Results and Discussion

5.1. Vegetation transmissivities and optical depth

Transmissivities $\Gamma^{p,\alpha}$ and uncertainties $\Delta\Gamma^{p,\alpha}$ of the vineyard vegetation in the winter state and the fully developed summer state were derived from $T_B^{p,\alpha}$ and T_{air} measured during the two-hour periods (11^{00} - 13^{00}) indicated in Figure 4. The radiative transfer approaches given in Section 4 solved for $\Gamma^{p,\alpha}$ were used with the parameter values {Y} and {ΔY} explained in Table 2. The resulting $\Gamma^{p,\alpha}$ for $30° \le \alpha \le 60°$, at horizontal (p = H, up triangles) and vertical (p = V, down triangles) polarization are depicted in Figure 6a for the assumptions $\omega^{p,\alpha}$ = 0 (large symbols) and $\omega^{p,\alpha}$ = 0.1 (small symbols). The error bars to the right of the large symbols (large caps) are the

[7] Predominant orientation of vegetation components (branches, stems, leafs) can lead to different propagation of horizontal and vertical field modes.

mean uncertainties $\Delta\Gamma^{p,\alpha}$ of single $\Gamma^{p,\alpha}$ (for $\omega^{p,\alpha}$ = 0) estimated from the uncertainties $\{\Delta Y\}$ using arithmetic error propagation (Section 4.2). The error bars to the left (smaller caps) of the large symbols represent the standard deviations $\sigma\Gamma^{p,\alpha}$ of the single $\Gamma^{p,\alpha}$ (for $\omega^{p,\alpha}$ = 0) derived from $T_B^{p,\alpha}$ and T_{air} measured for a given α. Panel b of Figure 6 shows optical depth $\tau^{p,\alpha}$ (again for the assumptions $\omega^{p,\alpha}$ = 0 and $\omega^{p,\alpha}$ = 0.1) diagonally through the vegetation computed from $\Gamma^{p,\alpha}$ using (8). The error bars to the right of the large symbols (large caps) are the mean uncertainties $\Delta\tau^{p,\alpha} = \Delta\Gamma^{p,\alpha} / \Gamma^{p,\alpha}$ of the single $\tau^{p,\alpha}$ (for $\omega^{p,\alpha}$ = 0), while the error bars to the left of the large symbols (smaller caps) are standard deviations $\sigma\tau^{p,\alpha}$ of the $\tau^{p,\alpha}$ (for $\omega^{p,\alpha}$ = 0) derived for specific α.

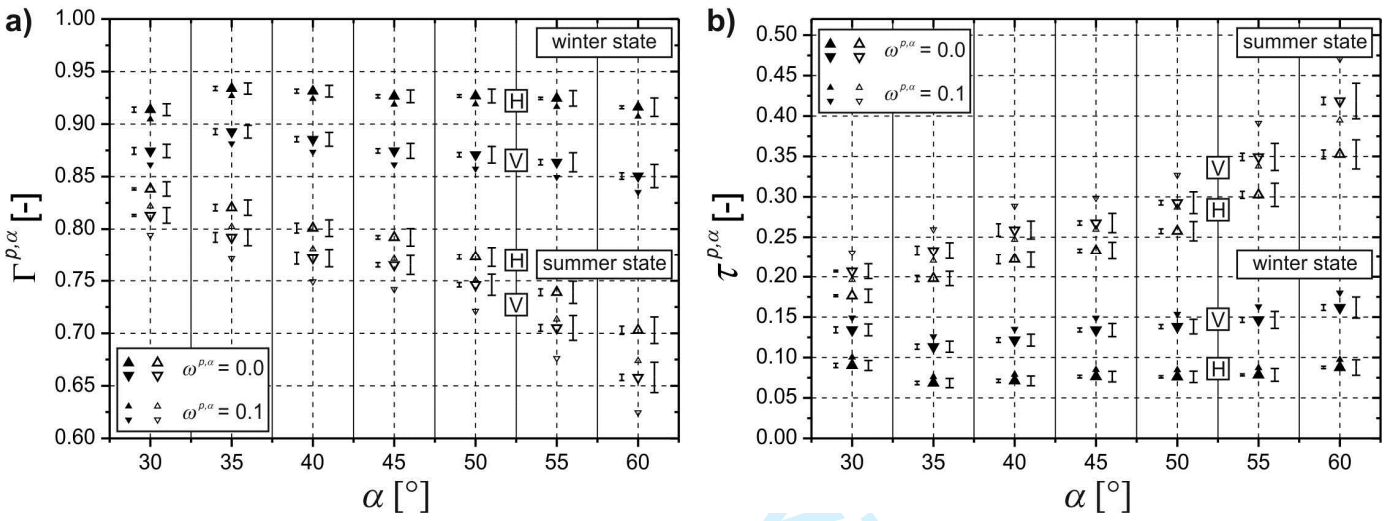

Figure 6: ***a)*** *Transmissivities $\Gamma^{p,\alpha}$ at horizontal (up triangles) and vertical (down triangles) polarization as functions of the observation angle α retrieved for the winter state and the summer state of the vegetation as functions of the observation angle α, and for horizontal (up triangles) and vertical (down triangles) polarization. $\Gamma^{p,\alpha}$ are derived assuming $\omega^{p,\alpha}$ = 0 (large symbols) and $\omega^{p,\alpha}$ = 0.1 (small symbols). The error bars to the right of the large symbols (large caps) are the mean uncertainties $\Delta\Gamma^{p,\alpha}$ of single $\Gamma^{p,\alpha}$. The error bars to the left of the large symbols (smaller caps) are the standard deviations $\sigma\Gamma^{p,\alpha}$ of the $\Gamma^{p,\alpha}$ measured for a given α.* ***b)*** *Vegetation optical depth $\tau^{p,\alpha}$ diagonally through the vegetation with errors bars corresponding to those in panel a).*

The angular dependency of the transmissivity $\Gamma^{p,\alpha}$ of the vegetation in the summer state (empty triangles) shows a clear decreasing trend with increasing α at H- and V-polarization. In the winter state, $\Gamma^{p,\alpha}$ is generally larger than in the summer state, and the angular dependence is less pronounced with a small decreasing trend for increasing α with $\alpha \geq 35°$. Furthermore, $\Gamma^{H,\alpha}$ is persistently larger than $\Gamma^{V,\alpha}$ for both vegetation states. The standard deviations $\sigma\Gamma^{p,\alpha}$ (error bars to the left of the large symbols) of the ≈ 160 samples $\Gamma^{p,\alpha}$ considered are smaller than the mean

uncertainties $\Delta\Gamma^{p,\alpha}$ (error bars to the right of the large symbols) estimated for the individual $\Gamma^{p,\alpha}$ with $\omega^{p,\alpha}$ = 0. This indicates that the assumptions made for the parameter uncertainties {ΔY} used to compute $\Delta\Gamma^{p,\alpha}$ by arithmetic error propagation (Section 4.2) are conservative enough to interpret $\Delta\Gamma^{p,\alpha}$ as upper boundaries of the uncertainties. To address concerns about the somewhat critical assumption $\omega^{p,\alpha}$ = 0 made in L-MEB retrievals applied to vineyards at VAS, the sensitivity of the $\Gamma^{p,\alpha}$ shown in Figure 6a with respect to the single scattering albedo $\omega^{p,\alpha}$ was analyzed. To this end, $\Gamma^{p,\alpha}$ were derived from the multiple-scattering emission model described in Section 4 assuming $\omega^{p,\alpha}$ = 0.1 (small triangles in Figure 6a), which is possible with specific types of low growing vegetation [38]. This accounts for vegetation volume scattering and results in an overall decrease in the estimated $\Gamma^{p,\alpha}$ (small symbols) in comparison with the $\Gamma^{p,\alpha}$ (large symbols) derived for the non-scattering vegetation ($\omega^{p,\alpha}$ = 0.0). Of course, all of the findings also apply to optical depth $\tau^{p,\alpha}$ shown in Figure 6b) if the definition (8) relating $\Gamma^{p,\alpha}$ to $\tau^{p,\alpha}$ is considered.

5.2. Comparison of vegetation parameters

As outlined in Section 4.3 the effects of vegetation anisotropy on the angular and polarization dependence of $\tau^{p,\alpha}$ were considered in the L-MEB retrievals by using (8) and the empirical approach (9) comprising the parameters τ_{NAD} and tt^{H}, tt^{V}. These values were quantified on the basis of the $\tau^{p,\alpha}$, shown in Figure 6b, by first applying (8) to correct the $\tau^{p,\alpha}$ for the elongation of the path through the vegetation layer. The resulting $\tau_0^{p,\alpha}$, shown in Figure 7 (the symbols are explained in Figure 6), were then used to minimize the objective function (10), yielding the values τ_{NAD}, and tt^{H}, tt^{V}. These values can be considered as “ground-truth”, and are therefore valuable for the SMOS calibration and validation activities taking place at the VAS site.

The $\tau_0^{p,\alpha}$ shown in Figure 7 reveal a decent decreasing trend with increasing α for the vegetation winter state. In contrast, a slightly increasing trend of $\tau_0^{p,\alpha}$ is evident for the summer state. This is qualitatively different from the angular dependency of $\tau^{p,\alpha}$ (Figure 6b), which still includes the effect of the increasing path length through the vegetation with increasing α. The

opposite angular trends of $\tau_0^{p,\alpha}$ observed for the two vegetation states indicate changing vegetation anisotropies in the course of vegetation development.

The bold solid and dashed lines in Figure 7 represent the empirical model $\tau_0^{p}(\alpha)$ given by (9), fitted to the $\tau_0^{p,\alpha}$ for the non-scattering vegetation ($\omega^{p,\alpha}$ = 0.0). The corresponding fine lines show $\tau_0^{p}(\alpha)$ fitted to $\tau_0^{p,\alpha}$ for $\omega^{p,\alpha}$ = 0.1. The best-fit values of the parameters τ_{NAD}, tt^H, tt^V to represent the angular dependency of $\tau_0^{p,\alpha}$ for the vegetation states considered with $\omega^{p,\alpha}$ = 0.0 and $\omega^{p,\alpha}$ = 0.1, respectively, are shown in Table 3. As can be seen, τ_0 retrieved for $\omega^{p,\alpha}$ = 0.0 and 0.1 of the vegetation in its fully developed summer state is increased by approximately 60% compared with τ_0 of the vegetation in the winter state. As a consequence of the still observable angular dependence of $\tau_0^{p,\alpha}$ (Figure 7), the values tt^p deviate from zero. Values tt^p < 1 represent increasing $\tau_0^{p,\alpha}$ with increasing α in accordance with the trend observed for the vegetation winter state. The values tt^p > 1 represent the opposite trend of $\tau_0^{p,\alpha}$, observed for the fully developed summer state of the vegetation. Furthermore, τ_{NAD} retrieved with the assumption $\omega^{p,\alpha}$ = 0.1 are slightly increased compared with τ_{NAD} retrieved without considering volume scattering ($\omega^{p,\alpha}$ = 0.0).

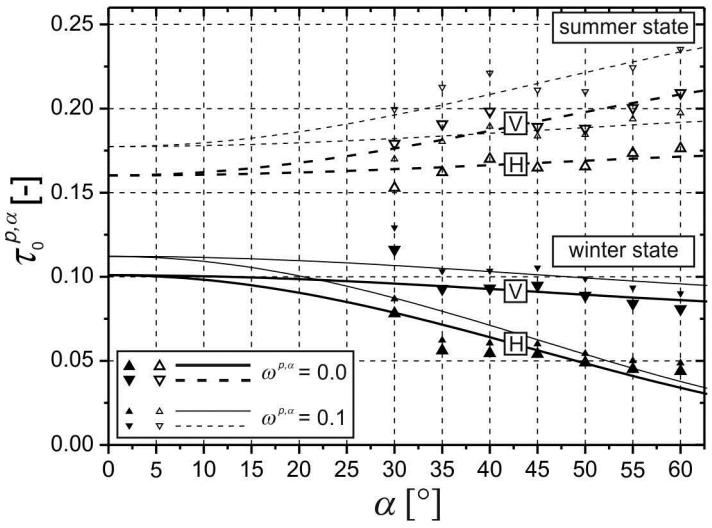

Figure 7: *Optical depths $\tau_0^{p,\alpha}$ derived from $\tau^{p,\alpha}$ shown in Figure 6b using (8). The symbols are in correspondance with those in Figure 6. The lines represent $\tau_0^{p}(\alpha)$ given by (9) with the best-fit values for τ_{NAD}, tt^H, tt^V shown in Table 3.*

Table 3: *Values of best fit-parameters τ_{NAD}, tt^H, tt^V derived with (10) to reproduce the $\tau_0^{p,\alpha}$ shown in Figure 7.*

Vegetation state:	$\omega^{p,\alpha}$	τ_{NAD}	tt^H	tt^V
Winter	0.0	0.101	0.116	0.804
Summer	0.0	0.160	1.093	1.401
Winter	0.1	0.112	0.116	0.805
Summer	0.1	0.177	1.108	1.423

The retrieved "ground-truth" values of τ_{NAD} (Table 3) obtained for the MELBEX III vineyard agree well with preliminary L-MEB retrievals applied to SMOS observation over the VAS area. During the winter state, the effective optical depth of the vine stocks τ_{NAD_STOCK} can be estimated as $\tau_{NAD\_STOCK} = b \cdot VWC_{STOCK}$, where b is a vegetation parameter and VWC_{STOCK} is the vegetation water content of the vine stocks. In the literature, the values of b are in the range 0.10 - 0.12 [11, 13, 39]. Values of VWC_{STOCK} were estimated by considering the stem density of 1/6 stocks m^{-2}, the moisture content of 0.5 m^3m^{-3}, and the average weight of vine stocks varying between 4 kg and 6 kg. With these assumptions, the VWC_{STOCK} is between 0.33 kg m^{-2} and 0.5 kg m^{-2}, and the resulting range of the effective optical depth of stocks is $0.033 \le \tau_{NAD\_STOCK} \le 0.06$. These values are approximately half the optical depth τ_{NAD} retrieved for the vegetation winter state based on the L-band measurements. If the range $0.101 \le \tau_{NAD} \le 0.112$ given in Table 3 is treated as the actual optical depth, the corresponding "ground truth" value of the b-parameter for the vineyard in its winter state would be in the range of $0.20 \le b \le 0.34$.

During the summer state, the water content of the fully developed vegetation was estimated to be 1.63 kg $m^{-2} \le VWC \le 1.8$ kg m^{-2}, to account for the different elements of the vine vegetation: stocks (0.33 kg m^{-2} - 0.5 kg m^{-2}), grapes (≈ 0.8 kg m^{-2}), stems (≈ 0.15 kg m^{-2}) and leaves (≈ 0.35 kg m^{-2}). If $0.10 \le b \le 0.12$, the estimated range of optical depth $\tau_{NAD} = b \cdot VWC$ for the vegetation summer state is $0.163 \le \tau_{NAD} \le 0.216$. These values agree well with the corresponding "ground-truth" values of τ_{NAD} for the fully developed vegetation state given in Table 3.

Another approach to estimate τ_{NAD} of the fully developed vine vegetation follows from an approximate relation used in the L-MEB model: $\tau_{NAD} \approx b' \cdot LAI$, where b' is a vegetation

parameter (the default value used in L-MEB is $b' = 0.06$) and *LAI* is the **L**eaf **A**rea **I**ndex. Two experiments carried out at the MELBEX III vineyard in 2009 and 2010 using destructive and non–destructive measurements (indirect optical estimations) converged to *LAI* yielded 2 m^2 $m^{-2} \leq LAI \leq 2.5$ m^2 m^{-2} for several representative vines. Based on these estimates, the vegetation optical depth of the fully developed vegetation is in the range $0.120 \leq \tau_{NAD} \leq 0.150$. However, the empirical relation $\tau_{NAD} \approx b' \cdot LAI$ used was developed for crop fields, and thus does not include any contributions from woody vine stocks. Nevertheless, the estimated range agrees well with the measurement based τ_{NAD} shown in Table 3, and also with the range $0.130 \leq \tau_{NAD} \leq 0.156$ estimated from the vegetation water content excluding vine stocks.

Considering the "ground-truth" values of the tt^p parameters (Table 3), tt^V exceeds tt^H for both vegetation states. These values indicate significant anisotropy of the vegetation, especially during the winter state (isotropy would correspond to $tt^V = tt^H = 1$). It is likely that these anisotropic effects can be related to the preferential orientation of the vine stocks in the vertical direction [13] as the other vegetation elements (stems, grapes, leaves) having no evident preferential orientation.

6. Summary and Conclusions

This study is the first to use data measured with one of the three identical ELBARA II radiometer systems required by ESA and developed by Gamma Remote Sensing (Gümligen, Switzerland, http://www.gamma-rs.ch/) within the framework of the ESTEC contract 21013/07/NL/FF "L-band Radiometer Systems to be deployed for SMOS Cal/Val Purposes". The corresponding multi-angular brightness temperatures were measured at the MELBEX III field site, which is situated in a vineyard. This land-use type is typical of about 75% of the VAS area, which is the Mediterranean validation and calibration site for SMOS retrievals. The study presented general aspects of ELBARA II for field applications, as well as the retrieval of radiative properties of vines based on ground-based L-band measurements in direct support of the ongoing SMOS calibration and validation activities at the VAS.

One major outcome of our study was the quantification of the absolute accuracy of ELBARA II measurements, which was shown to be better than ±1 K for a wide range of the scene brightness temperatures measured. The short-term measurements (foil experiments), for which radiative contributions of the soil were largely eliminated, revealed radiative properties of the vines at different development states that compared well with estimates based on vegetation parameters observed directly in the vineyard. For the trimmed vines during the winter state, the retrieved *b*-parameter was in the range of $0.20 \leq b \leq 0.34$. This is at least twice as much as the range $0.10 \leq b \leq 0.12$ often found in the literature for low growing vegetation. This discrepancy has to do with the fact that vines in their winter state consist mainly of woody components, which is not the case for most of low growing vegetation types investigated so far. Hence, we recommend using the higher values of the *b*-parameter found in this study for comparisons with SMOS retrievals over the VAS area. The multiple scattering radiative transfer model applied in our analysis also improves the physical base of the L-MEB retrieval scheme. In the case of very moist soils below scattering vegetation, this model potentially improves SMOS level-2 retrievals, while including the same set of parameters as the zero-order non-coherent solution of the radiative transfer equations currently implemented in L-MEB.

Acknowledgments

The authors would like to thank ESA for the loan of one of the three ELBARA II radiometers for deployment at the MELBEX III site (ESTEC ELBARA Loan Agreement 21013/07/NL/FF), and the Spanish Ministry for Science and Innovation (Spanish Research Programme on Space) for supporting the projects *Product Validation, Data Exploitation and Expert Center for the SMOS Mission* and *UVEG Part (MIDAS-5/UVEG)* and *Modeling of the Valencia Anchor Station Reference Area, SMOS Validation Core Area* (SMOS_Val@VAS). We are also grateful to Bodegas de Utiel, Finca El Renegado and Bodegas Iranzo, Finca Cañada Honda, in Caudete de las Fuentes for accommodating the MELBEX III experiment and for hosting the Valencia Anchor Stations (VAS) in their properties. The authors also acknowledge GAMMA Remote Sensing

Research and Consulting AG, Gümligen, Switzerland, for their assistance with setting up and maintaining the ELBARA II system. Furthermore, we thank Mr. O. Muggli from Alcan Packaging Services, Ldt., Neuhausen, Switzerland, for sponsoring the metalized foil, which was essential for this study. We also wish to express our thanks to Sandra Asensi, Amparo Coll and Alejandro Buil from the Climatology from Satellites Group and to Carmen Antolin, Cristina Millan, Fernando Requena and Elena Torre from the Center for Desertification Research, for their help with installing the foil under sometimes very tough conditions. Furthermore, we thank the TOSCA program of CNES (Centre National des Etudes Spatiales) for the financial support, and Silvia Dingwall for editing the manuscript.

References

[1] T. Schmugge, "Applications of passive microwave observations of surface soil moisture," *Journal of Hydrology,* vol. 212–213, p. 188−197, 1998.

[2] T. J. Jackson, *et al.*, "Soil moisture mapping at regional scales using microwave radiometry: the Southern Great Plains Hydrology Experiment," *IEEE Transactions on Geoscience and Remote Sensing,* vol. 37, pp. 2136-2150, 1999.

[3] E. G. Njoku, *et al.*, "Soil moisture retrieval from AMSR-E," *IEEE Trans. Geosci. Remote Sens.,* vol. 41, pp. 215-229, 2003.

[4] T. Schmugge, "Remote sensing of soil moisture," in *Encyclopedia of Hydrological Forecasting*, M. G. Anderson and T. Burt, Eds., ed Chichester: John Wiley & Sons, 1985, pp. 101-124.

[5] "SMOS Earth Explorers," *Available from: http://www.esa.int/esaLP/LPsmos.html,* 2000-2007.

[6] Y. Kerr, *et al.*, "Soil moisture retrieval from space: The soil moisture and ocean salinity (SMOS) mission," *IEEE Trans. Geosci. Remote Sensing,* vol. 39, pp. 1729-1735, 2001.

[7] M. Martin-Neira and J. M. Goutoule, " MIRAS—A two-dimensional aperture-synthesis radiometer for soil-moisture and ocean-salinity observations," *ESA Bull.,* vol. 92, pp. 95-104, 1997.

[8] Y. H. Kerr, *et al.*, "Soil moisture retrieval from space: The Soil Moisture and Ocean Salinity (SMOS) mission," *IEEE Trans. Geosci. Remote Sens.,* vol. 39, pp. 1729-1735, August 2001.

[9] C. Mätzler, *Thermal Microwave Radiation-Applications for Remote Sensing* vol. 52: IEE Electromagnetic Waves Series No. 52, London, UK, 2006.

[10] B. K. Hornbuckle, *et al.*, "Vegetation canopy anisotropy at 1.4 GHz," *IEEE Trans. Geosci. Remote Sensing,* vol. 41, pp. 2211 - 2223, Oct. 2003.

[11] T. Jackson and T. Schmugge, "Vegetation Effects on the Microwave Emission of Soils," *Remote Sens. Environ.,* vol. 36, pp. 203-212, 1991.

[12] Y. Kerr and E. G. Njoku, "A semiempirical model for interpreting microwave emission from semiarid land surfaces as seen from space," *IEEE Trans. Geosci. Remote Sensing,* vol. 28, pp. 384 - 393, May 1990.

[13] J.-P. Wigneron, *et al.*, "A simple algorithm to retrieve soil moisture and vegetation biomass using passive microwave measurements over crop fields," *Remote Sensing of Environment,* vol. 51, p. 331−341, 1995.

[14] M. Schwank, *et al.*, "L-Band Radiometer Measurements of Soil Water under Growing Clover Grass," *IEEE Trans. Geosci. Remote Sensing,* vol. 43, pp. 2225-2237, October 2005.

[15] A. A. Van de Griend and M. Owe, "Determination of microwave vegetation optical depth and single scattering albedo from large scale soil moisture and Nimbus/SMMR satellite observations," *International Journal of Remote Sensing,* vol. 14, p. 1875−1886, 1993.

[16] J.-P. Wigneron, *et al.*, "Two-D microwave interferometer retrieval capabilities of over land surfaces (SMOS Mission)," *Remote Sensing of Environment,* vol. 73, p. 270−282, 2000.

[17] P. de Rosnay, *et al.*, "SMOSREX: A long term field campaign experiment for soil moisture and land surface processes remote sensing," *Remote Sensing of Environment,* vol. 102, p. 377−389, 2006.

[18] A. Della Vecchia, *et al.*, "A Parametric Study About Soil Emission and Vegetation Effects for Forests at L-band," in *Geoscience and Remote Sensing Symposium, 2006. IGARSS 2006. IEEE International Conference on*, 2006, pp. 440-443.

[19] M. J. Escorihuela, *et al.*, "Effective soil moisture sampling depth of L-band radiometry: A case study," *Remote Sensing of Environment,* vol. 114, pp. 995–1001, 2010.

[20] P. Ferrazzoli, *et al.*, "Simulating L-band emission of forests in view of future satellite applications," *IEEE Transactions on Geoscience and Remote Sensing,* vol. 40, pp. 2700-2708, 2002.

[21] J. P. Grant, *et al.*, "Observations and Modeling of a Pine Forest Floor at L-Band," *IEEE Transactions on Geoscience and Remote Sensing,* vol. 47, pp. 2024-2036, 2009.

[22] K. Saleh, *et al.*, "Estimates of Surface Soil Moisture under Grass Covers using L-band Radiometry," *Remote Sensing of Environment,* vol. 109, pp. 42-53, 2007.

[23] K. Schneeberger, *et al.*, "Topsoil structure influencing soil water retrieval by microwave radiometry," *Vadose Zone Journal,* vol. 3, pp. 1169-1179, 2004.

[24] M. Schwank, *et al.*, "Testing a New Model for the L-band Radiation of Moist Leaf Litter," *IEEE Trans. Geosci. Remote Sensing,* vol. 46, pp. 1982-1994, 2008.

[25] J. Shi, *et al.*, "A Parameterized Surface Reflectivity Model and Estimation of Bare-Surface Soil Moisture with L-Band Radiometer," *IEEE Trans. Geosci. Remote Sensing,* vol. 40, pp. 2674-2686, 2002.

[26] I. Völksch, *et al.*, "L-Band Reflectivity of a Furrowed Soil Surface," *IEEE Trans. Geosci. Remote Sensing,* vol. 49, 2011.

[27] J.-P. Wigneron, *et al.*, "L-band Microwave Emission of the Biosphere (L-MEB) Model: Description and calibration against experimental data sets over crop fields," *Remote Sensing of Environment,* vol. 107, pp. 639–655, 2007.

[28] M. Schwank, *et al.*, "ELBARA II, An L-Band Radiometer System for Soil Moisture Research," *Sensors MDPI,* vol. 10, pp. 584-612, 2010.

[29] C. Mätzler, *et al.*, "ELBARA, the ETH L-band radiometer for soil-moisture research," *IGARSS '03. IEEE International Proceedings* vol. 5, pp. 3058-3060, 2003.

[30] T. Pellarin, *et al.*, "Two-year global simulation of L-band brightness temperatures over land.," *IEEE Trans. Geosci. Remote Sensing,* vol. 41, pp. 2135-2139, 2003.

[31] S. Misra, *et al.*, "CoSMOS: Performance of kurtosis algorithm for radio frequency interference detection and mitigation," *IGARSS conference proceedings* 2007.

[32] C. S. Ruf, *et al.*, "RFI detection and mitigation for microwave radiometry with an agile digital detector," *IEEE Trans. Geosci. Remote Sensing,* vol. 44, pp. 694-706, 2006.

[33] H. M. Pickett, *et al.*, "Characterization of a Dual-Mode Horn for Submillimeter Wavelengths," *IEEE transactions on Microwave and Techniques,* vol. 32, pp. 936- 937, August 1984.

[34] K. P. Kirdiashev, *et al.*, "Microwave radiation of the earth´s surface in the presence of vegetation cover," *Radioteknica,* vol. 24, pp. 256-264, 1979.

[35] T. Mo, *et al.*, "A model for microwave emission from vegetation-covered fields," *Journal of Geophysical Research,* vol. 87, p. 11.229–11.237, 1982.

[36] F. T. Ulaby, *et al.*, *Microwave remote sensing, active and passive, Vol I, Microwave remote sensing fundamentals and radiometry (1981), Vol II, Radar remote sensing and surface scattering and emission theory (1982), Vol III, From theory to applications' (1986)*: Artech House Inc., Noorwood, MA.

[37] C. Mätzler, *et al.*, *Thermal Microwave Radiation: Applications for Remote Sensing ser.*: London, U.K.: IET, 2006.

[38] J.-P. Wigneron, *et al.*, "Characterizing the dependence of vegetation model parameters on crop structure, incidence angle, and polarization at L-band," *IEEE Trans. Geosci. Remote Sensing,* vol. 42, pp. 416 - 425, Feb. 2004.

[39] A. A. V. d. Griend and J.-P. Wigneron, "The b-Factor as a Function of Frequency and Canopy Type at H polarization," *IEEE Trans. Geosci. Remote Sensing,* vol. 42, pp. 786-794, 2004.